Spontaneous formation of hole-selective contact and absorber for efficient perovskite solar cells

Xiaopeng Zheng[1†], Zhen Li[2†], Yi Zhang[4†], Min Chen[1†], Tuo Liu[5], Chuanxiao Xiao[1], Danpeng Gao[2], Jay B. Patel[1,3], Darius Kuciauskas[1], Artiom Magomedov[3,8], Rebecca A. Scheidt[1], Xiaoming Wang[7], Steven P. Harvey[1], Zhenghong Dai[6], Chunlei Zhang[2], Daniel Morales[3], Henry Pruett[5], Brian M. Wieliczka[1], Ahmad R. Kirmani[1], Nitin P. Padture[6], Kenneth R. Graham[5], Yanfa Yan[7], Mohammad Khaja Nazeeruddin[4], Michael D. McGehee[1,3], Zonglong Zhu[2*], Joseph M. Luther[1*]

[1]National Renewable Energy Laboratory, Golden, CO 80401, United States.

[2]Department of Chemistry and Hong Kong Institute for Clean Energy, City University of Hong Kong, Kowloon 999077, Hong Kong.

[3]Department of Chemical and Biological Engineering and Materials Science and Engineering, University of Colorado, Boulder, CO 80309, United States.

[4]Institute of Chemical Sciences and Engineering, École Polytechnique Fédérale de Lausanne (EPFL), Sion CH-1951, Switzerland.

[5]Department of Chemistry, University of Kentucky, Lexington, KY 40506, United States.

[6]School of Engineering, Brown University, Providence, RI 02912, United States.

[7]Department of Physics and Astronomy and Wright Center for Photovoltaics Innovation and Commercialization, University of Toledo, Toledo, OH 43606, United States.

[8]Department of Organic Chemistry, Kaunas University of Technology, Kaunas 50254, Lithuania.

[*]Corresponding author. Email: joey.luther@nrel.gov (J.M.L.); zonglzhu@cityu.edu.hk (Z.Z.)

[†] These authors contributed equally to this work.

Abstract: Simplifying the manufacturing processes of renewable energy technologies is crucial to lowering commercialization barriers. Here, we report for the context of perovskite solar cells (PSCs) that the hole-selective contact and perovskite light absorber can spontaneously form in one solution coating procedure for efficient inverted PSCs. By incorporating phosphonic or carboxylic acids directly into perovskite precursor solutions, we observe that the molecules self-assemble on the indium tin oxide substrate during perovskite film processing, forming a robust self-assembled monolayer (SAM) as an excellent hole-selective contact, along with crystallization of the perovskite. This solves a common wettability issue and simplifies device fabrication, advancing the manufacturability of PSCs. We obtained a power conversion efficiency of 24.5% for p-i-n geometry PSCs. The devices retained >90% of their initial efficiency after 1200 hours of operating at maximum power point under continuous illumination. The approach shows good generality as it is compatible with different SAM molecular systems, perovskites, solvents, and processing methods.

Perovskite solar cells (PSCs) have attained outstanding power conversion efficiency (PCE) approaching 26% due to the advances in compositional engineering[1], solvent engineering[2, 3], phase stabilization[4, 5], contact and interface engineering[6-10], and defect passivation[11-17]. These efficient PSCs are usually fabricated using multiple steps to sequentially deposit charge carrier transport layers, perovskite absorber, interfacial treatment layers, and electrodes. Reducing the number of device processing steps without sacrificing device efficiency is advantageous to reducing the complexity of process and manufacturing costs, which will aid in the manufacturability of PSCs.

In the inverted configuration, the use of p-type additives, such as 2,3,5,6-tetrafluoro-7,7,8,8-tetracyanoquinodimethane (F4TCNQ), fluorinated tetraarylbenzo [1,2-b:4,5-b′]dipyrrol-1,5-yl alkanediylsulfonate salt (BDPSO), and CuSCN, in perovskite precursor solution has been explored to remove the hole transport layer (HTL) deposition step by modifying the energetic alignment at the indium tin oxide (ITO)/perovskite interface [18-21]. This strategy achieved PSCs of 20.2% PCE [18]. However, despite this effort, this concept of HTL-free devices has not proliferated and the PCEs of HTL-free devices lag significantly behind those of regularly structured devices.

Recently, some of the most promising inverted PSCs have utilized a self-assembled monolayer (SAM) formed by carbazole-containing phosphonic acids (PAs), such as 2PACz ([2-(9H-carbazol-9-yl)ethyl]phosphonic acid), MeO-2PACZ ([2-(3,6-dimethoxy-9H-carbazol-9-yl)ethyl]phosphonic acid), and Me-4PACz ([4-(3,6-dimethyl-9H-carbazol-9-yl)butyl]phosphonic acid), as a hole-selective contact due to their ability to conformally coat rough surfaces and high selectivity of hole extraction with low interface electron trap density [22-27].

We report the spontaneous formation of both the SAM hole-selective contact and the absorber for efficient inverted PSCs. We introduced various molecules directly into the perovskite precursor solution and the molecules self-assembled as a SAM onto the ITO substrate during perovskite film processing, forming an excellent hole-selective contact. The devices are completed by passivating the top surface and applying the contacts, resulting in cells with a PCE of 24.5% with >1200 hours of stable operation under illumination. The approach is compatible with different molecules, perovskite compositions, solvent systems, and coating methods.

Perovskite film preparation and dynamic process of SAM formation

First, we show the procedure by using Me-4PACz, which is a PA with a carbazole body, incorporated into the precursor solution in 4:1 dimethylformamide (DMF):dimethyl sulfoxide (DMSO) solvent to make 1.56 eV bandgap $Cs_{0.05}(FA_{0.92}MA_{0.08})_{0.95}Pb(I_{0.92}Br_{0.08})_3$ (FA, formamidinium; MA, methylammonium) with various concentrations of Me-4PACz added between 0 and 2 mg/mL[13]. Throughout this manuscript, we will refer to a perovskite film that contained Me-4PACz in the precursor as the "target" perovskite and one without the PA as a "neat" perovskite. The target perovskite films were directly deposited on the ITO-coated glass substrate without the processing of an HTL. In parallel, we also prepared neat perovskite films on glass/ITO, glass/ITO/2PACz, and glass/ITO/Me-4PACz substrates. We observed that the perovskite films processed on ITO/Me-4PACz showed very poor coverage due to poor wetting, which may arise from methyl substitutions (**Supplementary Fig. 1**) [28], compared with perovskite films on ITO/2PACZ (**Supplementary Fig. 2**). The target perovskite film with Me-4PACz included in the precursor achieved full coverage on glass/ITO substrate comparable to the neat perovskite precursor directly deposited on glass/ITO substrate. There is no change in bandgap after introducing Me-4PACz (**Supplementary Fig. 3**). The top-view SEM images show that the average grain size of a perovskite film with Me-4PACz (0.5 mg/mL) is slightly larger than that of a neat perovskite film (**Supplementary Fig. 4**). We further increased the additive concentration to 2 mg/mL, which results in reduced grain size, indicating that there is an optimal concentration of the additive molecules for ideal crystallization. Dark current mapping by conductive atomic force microscopy (C-AFM) showed that the perovskite films with optimized Me-4PACz concentration showed the smallest dark current compared with both the neat film and the film with high Me-4PACz concentration (**Supplementary Fig. 5**).

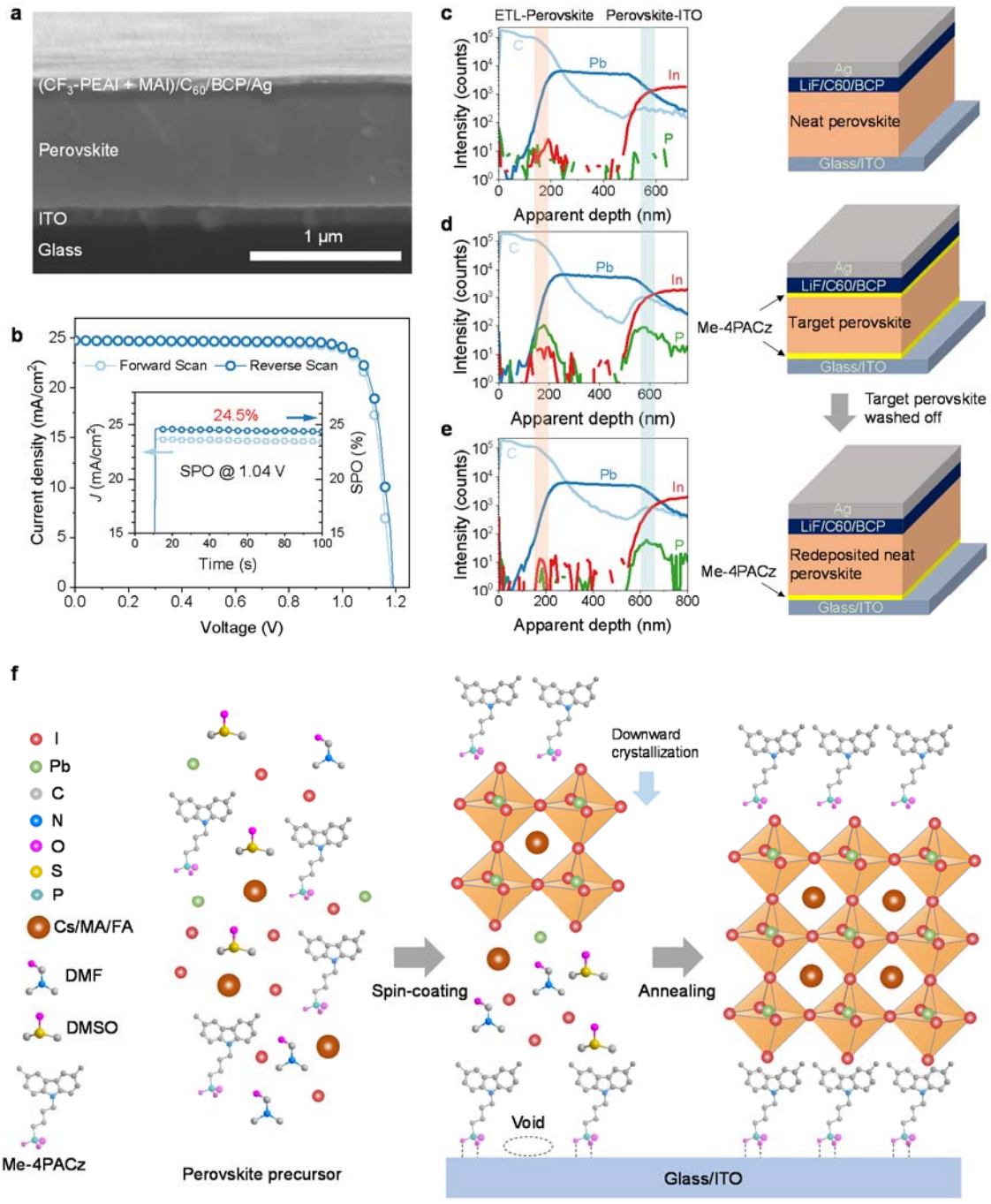

Fig. 1. Perovskite thin film preparation and characterization. *(**a**) SEM cross-section image of a target 1.55 eV PSC. (**b**) J-V curves of the champion target 1.55 eV PSCs. The inset shows the*

*stabilized power output (SPO). (**c** to **e**) TOF-SIMS profiling of 1.56 eV PSCs, along with a device stack diagram depicting the layers. A simplified device stack without surface passivation treatment was used. (c) Neat PSC. (d) Target PSC. (e) Target perovskite film was washed off, and a neat perovskite film was redeposited in a finished device. **(f)** Illustration of SAM formation and perovskite crystallization process.*

We fabricated inverted PSCs structured as glass/ITO/perovskite/passivation agent/C_{60}/BCP/Ag. The passivation agent is a mixture of 4-trifluorophenylethylammonium iodide (CF_3-PEAI) and methylammonium iodide (MAI) with 2:1 weight ratio[29, 30], and the $Cs_{0.05}(FA_{0.98}MA_{0.02})_{0.95}Pb(I_{0.98}Br_{0.02})_3$ perovskite films (E_G~1.55 eV) has a thickness about 800 nm (**Fig. 1a**). **Figure 1b** shows the forward and reverse current density-voltage (*J-V*) characteristics of a champion target 1.55 eV PSC with 24.5% PCE (confirmed with stabilized power output (SPO)). The Me-4PACz concentration-dependent *J-V* curves demonstrate that the optimal concentration for 1.55 eV devices is 0.25 mg/mL (**Supplementary Fig. 6**). At higher Me-4PACz concentration, the performance drops dramatically mainly because of reduced shunt resistance; The PCEs of devices with lower Me-4PACz concentrations decrease slightly mainly from the loss of V_{OC}, which we expect is the result of direct contact between the perovskite and ITO.

To gain an understanding of how and where the Me-4PACz SAM forms, we used a simplified device stack without a surface passivation treatment, structured as glass/ITO/perovskite (1.56 eV)/LiF/C_{60}/BCP/Ag, for optical and structural characterizations, unless otherwise noted. The thickness of the perovskite films is about 650 nm (**Supplementary Fig. 7**). The Me-4PACz concentration-dependent *J-V* curves demonstrate that the PCEs of the 1.56 eV PSCs are highest

when the concentration is between 0.25 and 1 mg/mL (**Supplementary Fig. 8**), and the devices deliver a PCE of 22.6% (**Supplementary Fig. 9**).

We then characterized these devices using depth profiling with time-of-flight secondary ion mass spectrometry (TOF-SIMS) (**Fig. 1c** to **1e**). For the target perovskite film, a pronounced phosphorous (P) signal from the Me-4PACz is located at both the ITO-perovskite interface and the perovskite-electron transport layer (ETL) interface (**Fig. 1d**), which indicates that the Me-4PACz molecules are excluded to the top and bottom interface during the perovskite film processing. We then removed the target perovskite film by dissolving it in dimethylformamide (DMF), which yielded an optically clear substrate. We then redeposited a neat perovskite film and performed TOF-SIMS again. We still observed a P signal of similar magnitude at the ITO-perovskite interface when depth profiling this new film deposited without Me-4PACz additive (**Fig. 1e**). This result was further confirmed with X-ray photoelectron spectroscopy (XPS, **Supplementary Fig. 10**), showing the presence of P on the ITO surface with the target perovskite film washed off. The TOF-SIMS and XPS results suggest that Me-4PACz SAMs formed on ITO during the perovskite film processing due to the strong bond between PAs and ITO.

Seeking to investigate the dynamic process of SAM formation, we also performed experiments to wash off the perovskite intermediate-phase film containing Me-4PACz using DMF while still partially wet. We then redeposited a neat perovskite film on the substrate (**Fig. 2a**). The resulting device shows a PCE of only 18.4% (**Fig. 2b**). The cell was inferior in performance to a target device (V_{OC} of 1.08 V vs. 1.14 V and FF of 78.9% vs. 83.3%) indicative of SAM-free regions

leading to direct contact between the ITO and perovskite. Here we conclude that prior to the perovskite crystallization, the SAM is loosely packed and incomplete.

We further fabricated neat PSCs on the substrate with the target perovskite film washed off after full crystallization. The resulting device shows a much higher PCE (21.7%) with a V_{OC} of 1.12 V, compared with the neat devices fabricated on the ITO substrate with intermediate-phase film containing Me-4PACz washed off. This result demonstrates that a denser and robust SAM formed on the ITO substrate during the perovskite film crystallization process. Perovskite films have been shown to follow a top-to-bottom downward crystallization process initialized by the evaporation of residual solvent from the top surface of "wet" films[31]. We surmise that the Me-4PACz gets pushed downward and concentrated on the ITO surface during the film formation. The phosphonic acid headgroups bind strongly to the ITO substrate spontaneously forming a robust SAM [32]. Residual Me-4PACz is present on the perovskite top surface. Me-4PACz is too large to be incorporated into the lattice and we do not see a substantial P signal throughout the film but cannot rule out a very small amount at grain boundaries. The 1.55 eV PSCs also showed a similar SAM formation process (**Supplementary Fig. 11**).

Figure 1f shows the schematic illustration of dynamic process of SAM formation. Some Me-4PACz molecules bind to the ITO surface via covalent bond/chemisorption and form a loosely packed SAM during the perovskite precursor application, but a denser and robust SAM forms during the perovskite film crystallization process.

We further performed *in situ* real-time photoluminescence (PL) to monitor the perovskite crystallization process (**Supplementary Fig. 12**). The result shows that the formation of the neat and target film is similar, and the target film has overall higher PL intensity during crystallization, indicating fewer defects in the target perovskite film.

Characterization of perovskite films and interfaces

Given the ability to simultaneously form a SAM and perovskite layer and then remove only the perovskite layer with DMF, we further examined the electronic structure of ITO substrates and perovskite films by ultraviolet photoelectron spectroscopy (UPS). We washed off the perovskite films and compared the work function (Φ) of the ITO substrates. We observed a significant change in the Φ from 4.33 eV (identical to that of bare ITO) for the ITO substrates after rinsing away the neat perovskite to 4.94 eV for the ITO substrates with removed target perovskite (**Fig. 2c**). Density functional theory (DFT) calculations show that the electric dipole moment of Me-4PACz increases the work function of the ITO surface (**Supplementary Fig. 13** and **Supplementary Fig. 14**). We also detected a clear signature from the Me-4PACz SAM on ITO with a highest-occupied molecular orbital (HOMO) of 5.59 eV for the ITO substrate after rinsing away the target perovskite (**Fig. 2d**). The Φ of the top of the perovskite film also increases from 4.54 (neat) to 4.66 eV (target) (**Fig. 2e**), and the valence band maximum (VBM) changes from 5.88 (neat) to 5.74 eV (target) (**Fig. 2f**), revealing that the target perovskite film becomes less n-type compared with the neat film (**Fig. 2g**). The VBM of the modified perovskite aligns well with that of the HOMO of Me-4PACz on the ITO substrate after the target perovskite is washed away. Therefore, Me-4PACz likely promotes extraction of the photo-generate holes at the perovskite-ITO interface while also serving to increase the selectivity of the contact.

We next used cross-sectional Kelvin probe force microscopy (KPFM) to probe the charge carrier extraction barriers at the bottom interface (ITO/perovskite)[33, 34]. The first derivative of the potential difference (measured between the probe and cross-section surface of the sample) shows the electric-field distribution relative to the metallurgical interfaces. Previously we found that the main junction is located at the perovskite-ETL interface with a potential barrier at the HTL-perovskite interface[33]. Here, we observed a significant potential barrier at the ITO/perovskite interface induced by a mismatch of energetic alignment on the ITO/perovskite (neat) interface (**Supplementary Fig. 15**). The potential barrier at the ITO/perovskite interface is remarkably reduced for the target perovskite film, which could facilitate the hole extraction at the ITO/perovskite interface. To gain an understanding of the impact of SAMs on the charge carrier separation and transport at the top interface (perovskite/ETL), we analyzed the direction of the interface dipole induced by Me-4PACz (**Supplementary Fig. 16**). PAs have been shown to also anchor to the perovskite film surface with the alkyl tail pointing upward[35]. The molecular dipole induced by Me-4PACz on the top surface would thus have the same polarity as below the perovskite and could promote electron extraction to the ETL. Thus, contrary to a conventional HTL (such as PTAA, Spiro-OMeTAD, etc.), SAMs can be present on both sides of the perovskite absorber provided that the dipole is pointing in the same direction to promote charge carrier extraction at both interfaces (**Supplementary Fig. 16**).

We performed time-resolved photoluminescence (TRPL) with the perovskite films on glass and glass/ITO/PTAA substrates. TRPL for the perovskite films on glass substrates showed that the perovskite film with 0.5 mg/mL Me-4PACz has the longest average lifetime (τ_{ave}) of 520.5 ns

compared with 305.0 ns for neat perovskite film (**Fig. 2h** and **Supplementary Table 1**), which suggests that Me-4PACz reduces surface nonradiative recombination. We also measured TRPL for the perovskite films with and without Me-4PACz on glass/ITO/PTAA substrates and fitted the results with a bi-exponential decay equation. If we assume τ_1 is dominant by charge extraction to the transport layers and τ_2 is dominant by interface recombination, as the assignments of the fast decay and slow decay in the literature[36], the target perovskite film on ITO/PTAA shows shorter τ_1, indicating faster hole-extraction, and longer τ_2, indicating the reduced interface recombination (**Supplementary Fig.17** and **Supplementary Table 2**). Tan et al. reported that 2PACz efficiently passivates deep traps in perovskite because of the chemical bonding between Pb and O from the phosphoryl group of the 2PACz[37]. Another PA additive, 2-aminoethylphosphonic acid, has been demonstrated to passivate positively charged defects (such as iodine vacancies (V_I) and lead−iodine antisites (Pb_I)) and therefore improve the device efficiency and durability[38].

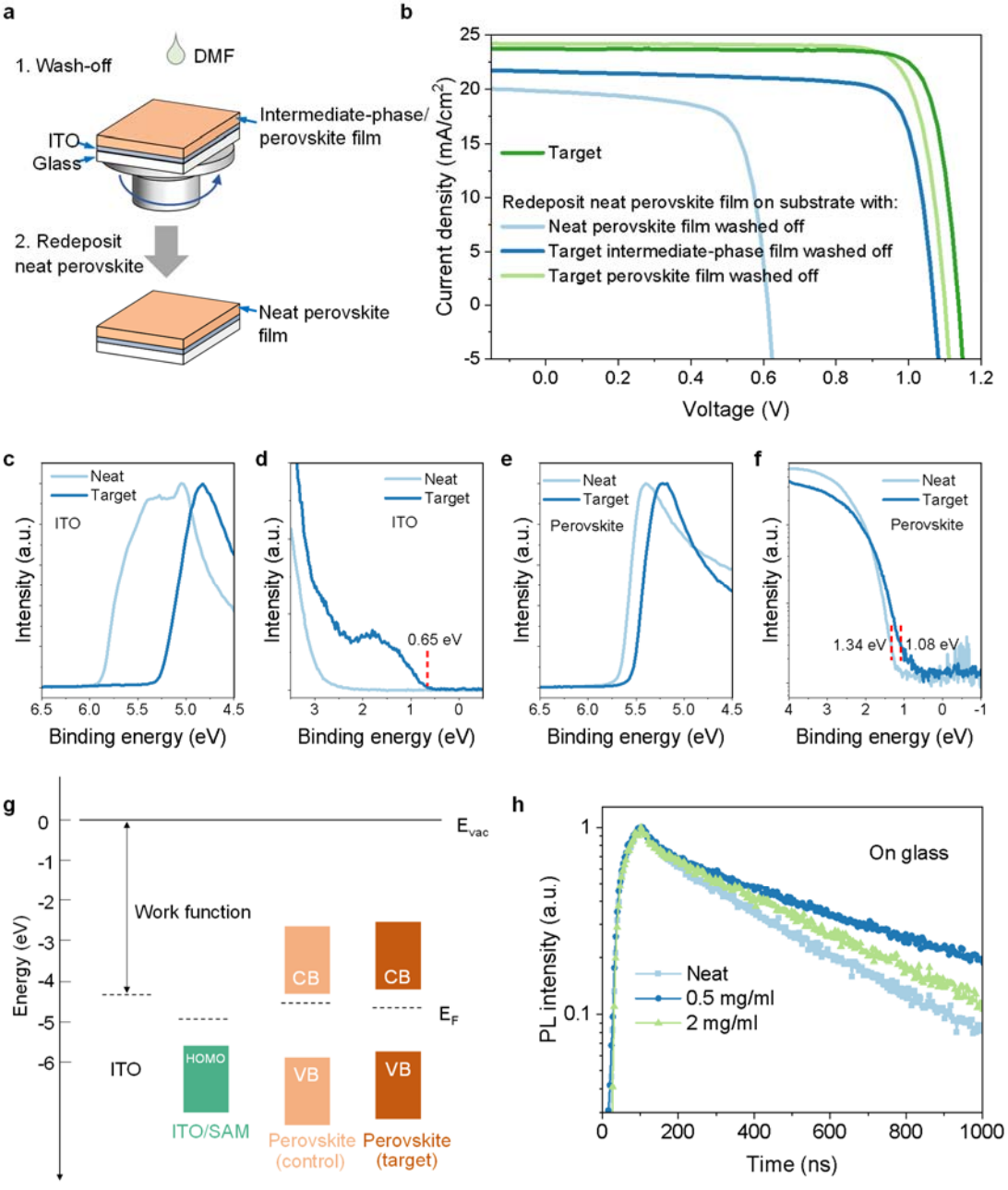

220

221 ***Fig. 2. Characterization of SAM formation, energetic alignment, and carrier lifetime.*** *(**a**)*

222 *Schematic illustration of intermediate-phase/perovskite film washing off and neat perovskite film*

223 *redeposition process. (**b**) J-V characteristics of the neat PSCs fabricated on substrates with*

224 *intermediate-phase/perovskite film washed off. (**c** to **f**) UPS (10.2 eV excitation) of the secondary*

225 *electron cutoff (c) and valence band (d) regions of the ITO and ITO/SAM substrates after washing*

*off the neat perovskite and target perovskite film, respectively. UPS of the secondary electron cutoff (e) and valence band (f) regions of the neat and target perovskite films, respectively. (**g**) Energy-level scheme extracted from UPS. (**h**) TRPL of perovskite films with different Me-4PACz concentrations on glass substrates.*

PV performance and stability

We tested this approach on a wide bandgap composition $Cs_{0.05}FA_{0.8}MA_{0.15}Pb(I_{0.75}Br_{0.25})_3$ (E_G~1.68 eV), which is commonly used for perovskite-silicon tandem solar cells[25], to demonstrate the generality of this concept. The target device showed a PCE of 20.3% with a V_{OC} of 1.14 V from the reverse scan (**Supplementary Fig. 18**). Using a quasi-Fermi level splitting (QFLS) approach, we found that after covering the perovskite with C_{60}, consistent with previous reports[37], both ITO/Me-4PACz/neat perovskite and ITO/target perovskite stacks showed room for possible improvement of the voltage by 65-80 mV (**Fig. 3a**). We ascribe this to incomplete passivation of defect states on the perovskite surface. To confirm, we thereafter passivate the perovskite surface using a mixture of CF_3-PEAI and MAI to further improve the device efficiency[29, 30]. XPS result confirms the co-existence of Me-4PACz and CF_3-PEAI on the perovskite surface (**Supplementary Fig. 19**). The PCE of the 1.68 eV PSCs was improved to 21.6% with a V_{OC} of 1.19 V, after surface passivation (**Supplementary Fig. 20**). We also applied this approach in a 1.8 eV perovskite composition ($Cs_{0.15}FA_{0.85}Pb(I_{0.6}Br_{0.4})_3$) which is commonly used as a front cell for all-perovskite tandems[39], and the target 1.8 eV devices showed a PCE of 18.6% with a high V_{OC} of 1.29 V (**Supplementary Fig. 21**).

A PCE of 24.5% with a high V_{OC} of 1.19 V was also achieved for 1.55 eV PSCs with surface passivation, along with a J_{SC} of 24.78 mA/cm^2 and FF of 83.1% from the reverse scan (**Fig. 1b** and **Fig. 3b**). The 24.5% PCE represents a significant improvement over the previous highest reported PCEs for HTL-free PSCs, and within one percentage point of the highest PCE for inverted PSCs (**Supplementary Table 3**). The narrow PCE distribution confirms good reproducibility (**Supplementary Fig. 22** and **Supplementary Table 4**). The external quantum efficiency (EQE) was integrated against the solar spectrum to estimate a J_{SC} of 24.6 mA/cm^2 in agreement with the *J-V* measurement (**Supplementary Fig. 23**).

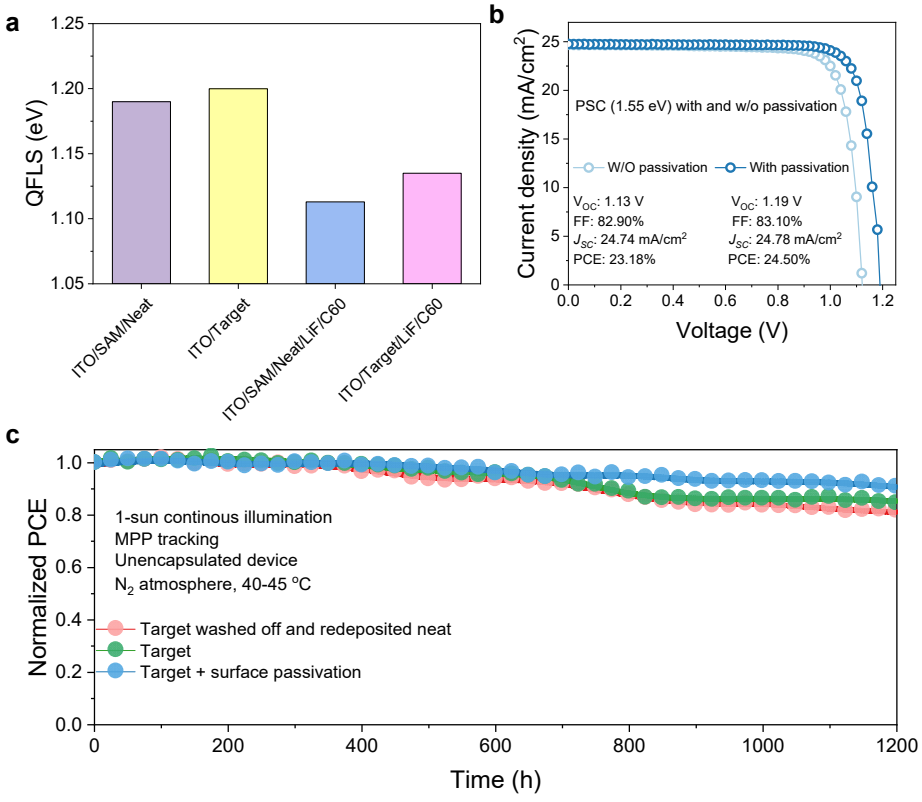

Fig. 3. Device photovoltaic characteristics and stability. *(**a**) The calculated QFLS of the glass/ITO/Me-4PACz/neat perovskite, glass/ITO/target perovskite, glass/ITO/Me-4PACz/neat perovskite/LiF/C_{60}, and glass/ITO/target perovskite/LiF/C_{60}. (**b**) J-V curves of the target 1.55 eV PSCs with and without surface passivation. (**c**) Operational stability of neat 1.55 eV PSC*

fabricated on the substrate with target perovskite washed off, and target 1.55 eV PSC with and without surface passivation. Normalized PCE as a function of time under the following conditions: 1-sun continuous illumination, MPP tracking, unencapsulated, N_2 atmosphere, and operating cell temperature of ~40-45 ^oC.

We evaluate the operating stability using maximum power point (MPP) tracking of the unencapsulated 1.55 eV devices under continuous illumination (**Fig. 3c**). The neat device fabricated on the substrate with target perovskite washed off, with Me-4PACz only on the bottom interface, retained 82% of initial PCE after 1200 hours of continuous operation. The target devices with and without surface passivation, with Me-4PACz on both the bottom and top interface, retained 91% and 85% of initial PCE, respectively.

Blade-coating of PSCs and evaluation of different PAs

Encouraged by the high device performance, we further evaluated the film uniformity and upscaling capability by making PSCs via blade-coating. Due to severe wetting issues of trying to process perovskites directly onto Me-4PACz SAM, we observed that there is almost no perovskite remaining on the ITO/Me-4PACz substrate (**Fig. 4a**). By contrast, the blade-coated target perovskite film with Me-4PACz included in the precursor achieved full coverage on glass/ITO substrate (**Fig. 4b**). A 1-cm^2 blade-coated target device achieved a PCE of 22.5% from the reverse scan, with a V_{OC} of 1.16 V, a J_{SC} of 23.88 mA/cm^2, and a FF of 81.23%. (**Fig. 4c**). The SPO efficiency is 22.1%. The narrow PCE distribution confirms good reproducibility (**Supplementary Fig. 24**) and this overcomes a manufacturability challenge of poor wetting from perovskite inks on a SAM-coated surface.

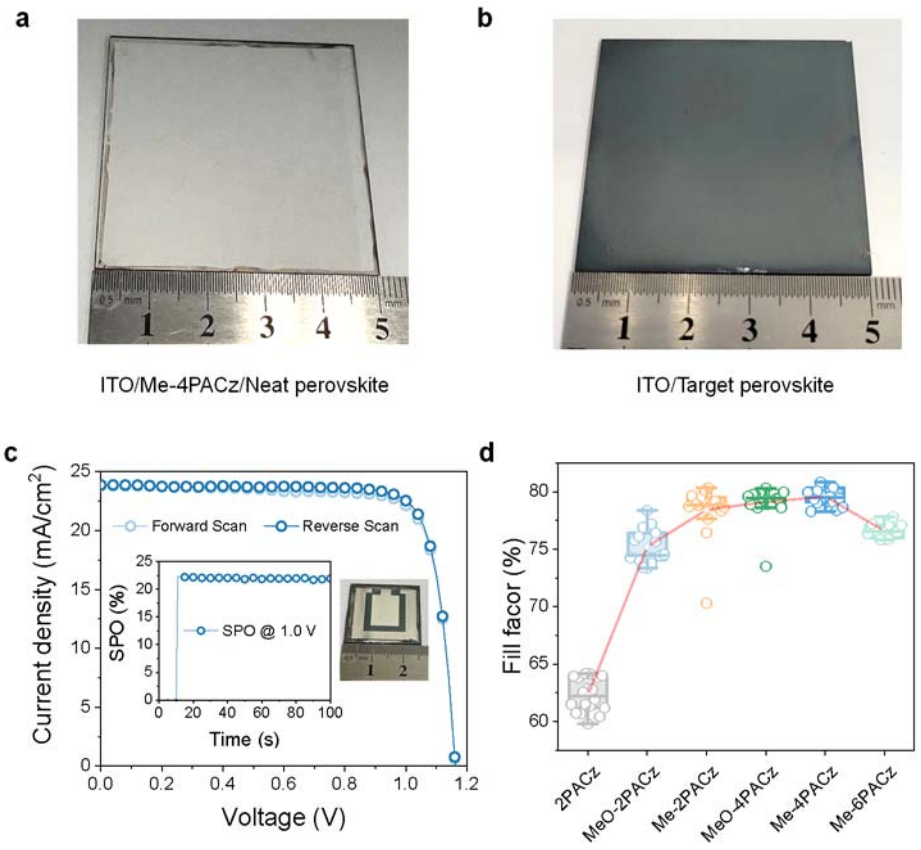

Fig. 4. Blade-coating of PSCs and evaluation of different PAs. ***(a, b)*** *Photographic images of blade-coated (a) neat 1.55 eV perovskite film on ITO/Me-4PACz SAM, and (b) target 1.55 eV perovskite film on ITO.* ***(c)*** *J-V curves of the champion 1-cm² blade-coated 1.55 eV PSC with surface passivation. The inset shows the stabilized power output (SPO) and the photographic image of a 1-cm² blade-coated target device.* ***(d)*** *Comparison of fill factor values of spin-coated 1.56 eV PSCs fabricated with different PAs in the perovskite precursor.*

To understand why Me-4PACz enables the spontaneous formation of a robust SAM during perovskite film processing, we compared the photovoltaic (PV) parameters of the 1.56 eV PSCs fabricated with different PAs (2PACz, MeO-2PACZ [(2-(3,6-dimethoxy-9H-carbazol-9-yl)ethyl)phosphonic acid], Me-2PACz [(2-(3,6-dimethyl-9H-carbazol-9-yl)ethyl)phosphonic

acid], MeO-4PACz [(4-(3,6-dimethoxy-9H-carbazol-9-yl)butyl)phosphonic acid], Me-4PACz, and Me-6PACz [(6-(3,6-dimethyl-9H-carbazol-9-yl)hexyl)phosphonic acid]) incorporated in the perovskite precursor (**Fig. 4d**, **Supplementary Fig. 25**, and **Supplementary Fig. 26**). The devices with smaller PA (2PACz) show low PV merits (J_{SC} (21.5-22.5 mA/cm^2), V_{OC} (0.9-1.06 V), FF (60-65%), and PCE (11.5-14.5%)). When the size of the SAM molecules becomes larger by introducing two methyl or methoxy groups, we observed improved device FF to ~75% for MeO-2PACZ and ~78% for Me-2PACz due to better coverage of the SAM on ITO corresponding to better hole extraction. The FF is further improved to ~79% and ~80% for the devices with PAs with longer alkyl spacer, MeO-4PACz and Me-4PACz, respectively. This result indicates that the larger Me-4PACz molecules are more efficiently repelled to the ITO/perovskite interface and the stronger lateral van der Waals interactions help organize the molecules into high grafting density[40] and well-ordered SAM[40, 41]. Further increasing the spacer alkyl chain length to 6 for Me-6PACz reduced the FF and PCE due to the detrimental impact of a long spacer on charge extraction[23, 42].

The generality of the approach

We have demonstrated the generality of the approach above in terms of various perovskite compositions, SAM chemistry, and processing method (both solvent system used and coating procedure). We tested different SAM molecular systems and solvents. PSCs fabricated with carboxylic acid SAM molecule (EADR03, 4-(3,6-bis(2,4-dimethoxyphenyl)-9H-carbazol-9-yl)benzoic acid)[43-45] or phosphonic acid SAM molecule with phenothiazine electron-rich group (Br-2EPT, (2-(3,7-dibromo-10h-phenothiazin-10-yl)ethyl)phosphonic acid)[46] incorporated in the perovskite precursor delivered similar PCEs compared with the devices fabricated by “layer by

layer" deposition method, demonstrating the generality of the approach in terms of SAM molecular system (**Fig. 5a, b**).

Acetonitrile (ACN) with 2-methoxyethanol (2-ME) is a solvent system widely used in scalable blade-coating of PSCs[47, 48]. Due to the limited solubility of CsI in the solvent, we used Cs-free perovskite composition ($FA_{0.98}MA_{0.02}Pb(I_{0.98}Br_{0.02})_3$). **Figure 5c inset** shows the photographic image of the perovskite precursor with Me-4PACz dissolved in a mixed solvent of ACN and 2-ME, and a perovskite film prepared by blade-coating of the precursor. The target PSCs with Me-4PACz fabricated by blade-coating using ACN:2-ME showed a PCE of 22.1% from the reverse scan (**Fig. 5c**).

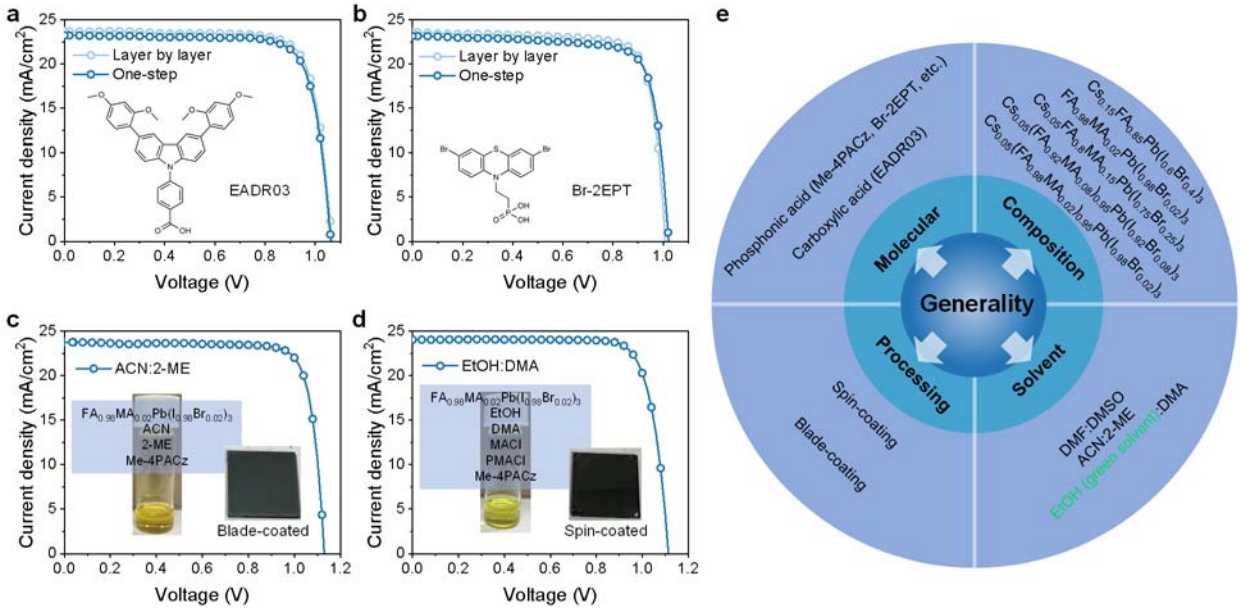

Fig. 5. Evaluation of different SAM molecular systems and solvents. *(**a**) J-V curves of the target 1.55 eV PSCs and PSCs fabricated by "layer by layer" method using 4-(3,6-bis(2,4-dimethoxyphenyl)-9H-carbazol-9-yl)benzoic acid (EADR03) SAM molecule. The inset shows the chemical structure of EADR03 SAM molecule. (**b**) J-V curves of the target 1.55 eV PSCs and PSCs*

*fabricated by "layer by layer" method using (2-(3,7-dibromo-10h-phenothiazin-10-yl)ethyl)phosphonic acid (Br-2EPT) SAM molecule. The inset shows the chemical structure of Br-2EPT SAM molecule. (**c**) J-V curve of a blade-coated target $FA_{0.98}MA_{0.02}Pb(I_{0.98}Br_{0.02})_3$ PSC using ACN:2-ME as a solvent. The inset shows the photographic image of the perovskite precursor with Me-4PACz dissolved in a mixed solvent of ACN and 2-ME, and a perovskite film prepared by blade-coating of the precursor. (**d**) J-V curve of a spin-coated target $FA_{0.98}MA_{0.02}Pb(I_{0.98}Br_{0.02})_3$ PSC using EtOH:DMA as a solvent. The inset shows the perovskite precursor with Me-4PACz dissolved in a mixed solvent of EtOH and DMA, and a perovskite film prepared by spin-coating of the precursor. (**e**) Summary of the generality of the approach.*

Yun et al. demonstrated a greener solvent system based on ethanol (EtOH) that yields high performance without the need of DMF or ACN which may impede the sustainability aspects of PSCs[49, 50]. We further explored the EtOH-based green solvent to improve both PSC manufacturability and sustainability. EtOH or isopropanol is the solvent commonly used for the deposition of SAM layer via spin-coating or dipping method[22]. Following the previous report[50], we were able to dissolve the perovskite precursor in an EtOH-based solvent. Due to the limited solubility of CsI in the solvent, we used Cs-free perovskite composition ($FA_{0.98}MA_{0.02}Pb(I_{0.98}Br_{0.02})_3$). **Figure 5d inset** shows the photographic image of the perovskite precursor with Me-4PACz dissolved in a mixed solvent of EtOH and dimethylacetamide (DMA), and a perovskite film prepared by spin-coating of the precursor. The target PSCs with Me-4PACz fabricated by spin-coating using an EtOH-based green solvent showed a PCE of 21.6% from the reverse scan (**Fig. 5d**).

Figure 5e summarized the generality of the approach. This approach is compatible with different SAM molecular systems (carbazole- and phenothiazine-based) with both a phosphonic acid and carboxylic acid headgroup, along with multiple (5) compositions of perovskites, solvents (DMF:DMSO, ACN:2-ME, and an ethanol-based green solvent), and processing methods (spin-coating and scalable blade-coating). Further fine optimization of the approach for each condition when using different SAM molecular systems, perovskites, solvents, and processing methods, will enable for obtaining higher device performance.

Conclusion

In summary, we have demonstrated that the incorporation of SAM molecules directly into the perovskite precursor enabled a spontaneous deposition of both the hole-selective SAM and the perovskite layer. Our approach emphasizes the synergetic roles of molecular size, dipole direction, dipole strength, energetic alignment, and defect passivation of the perovskite by PAs. Incorporating the SAM molecules into several different types of perovskite precursor solves a critical wetting issue of processing perovskite onto SAM while simplifying the manufacturability and retaining high efficiency when proper defect passivation is applied. The approach is versatile as it allows for the use of different SAM molecules, perovskites, solvents, and coating methods, for improving PSC manufacturability and sustainability.

Methods

Materials. Formamidinium iodide (FAI), methylammonium iodide (MAI), and methylammonium bromide (MABr) were purchased from Greatcell Solar. 4-trifluorophenylethylammoniumiodide (CF_3-PEAI) was purchased from Xi'an Polymer Light Technology. Lead iodide (PbI_2, ultra dry,

99.999%) was purchased from Alfa Aesar. Lead bromide ($PbBr_2$, 99.999%), cesium iodide (CsI, 99.999%), lithium fluoride (LiF, ≥99.98%), anhydrous dimethylformamide (DMF), anhydrous dimethyl sulfoxide (DMSO), and anhydrous chlorobenzene (CB) were purchased from Sigma-Aldrich. 2PACz and Me-4PACz were purchased from Tokyo Chemical Industry (TCI)-America. MeO-2PACz, Me-2PACz, MeO-4PACz, Me-4PACz, Me-6PACz, EADR03, Br-2EPT, C_{60}, and bathocuproine (BCP) were purchased from Luminescence Technology Corp. (Lumtec). All chemicals were used as received without further purification.

Device fabrication. The patterned glass/ITO substrates were sequentially cleaned with acetone and isopropanol under ultrasonication, and then dried with nitrogen and treated with UV-ozone for 15 min. In a typical procedure, perovskite precursor solution (1.7 M $Cs_{0.05}(FA_{0.98}MA_{0.02})_{0.95}Pb(I_{0.98}Br_{0.02})_3$ for 1.55 eV cells, or 1.4 M $Cs_{0.05}(FA_{0.92}MA_{0.08})_{0.95}Pb(I_{0.92}Br_{0.08})_3$ for 1.56 eV cells, or 1.5 M $Cs_{0.05}FA_{0.8}MA_{0.15}Pb(I_{0.75}Br_{0.25})_3$ for 1.68 eV cells) was dissolved in a mixed solvent (DMF/DMSO = 4:1 v/v ratio) in a nitrogen glovebox. For the target device, Me-4PACz was added to the perovskite precursor. 2 mg/mL Me-4PACz stock solution was prepared by adding 2 mg Me-4PACz powder into 1 mL perovskite precursor. We then mixed 2 mg/mL stock solution with neat perovskite precursor (1:3 or 1:7 v/v ratio) to get 0.5 or 0.25 mg/mL Me-4PACz perovskite precursor. The hole-selective contact and perovskite absorber were cast in a single coating step in a nitrogen glovebox. The perovskite precursor containing Me-4PACz was spin-coated on UV-ozone treated glass/ITO substrates at 2000 rpm for 2 s and 4000 rpm for 20 s, and 150 µL CB was dropped on the spinning substrate 5s before the end of the spin-coating process. Subsequently, the sample was annealed at 100 °C for 30 min. For the devices with surface passivation treatment, a mixture of 4-

trifluorophenylethylammoniumiodide (CF_3-PEAI, 2 mg/mL) and MAI (1 mg/mL) was dissolved in a mixed solvent of IPA: DMF (v/v ratio of 150:1) and dynamically spun on the as-prepared perovskite films at 5000 rpm for the 30 s, then annealing for 100 ℃, 10 min. The devices with surface treatment were finished by thermally evaporating C_{60} (25 nm), BCP (6 nm), and silver (100 nm) in sequential order. For the devices without surface passivation treatment, we sequentially deposited LiF (1nm), C_{60} (25 nm), BCP (6 nm), and silver (100 nm) to finish the device.

For 1.80 eV PSC fabrication, 1.2 M perovskite precursor solution was prepared by mixing CsI, CsBr, FAI, FABr, PbI_2, and $PbBr_2$ according to a chemical formula of $Cs_{0.15}FA_{0.85}Pb(I_{0.6}Br_{0.4})_3$. 8-10 mol% of excess PbI_2 was added. Me-4PACz was added in perovskite precursor with a concentration of 0.25 mg/mL. The hole-selective contact and perovskite absorber were cast in a single coating step in a nitrogen glovebox. In a typical procedure, the perovskite precursor containing Me-4PACz was spin-coated on UV-ozone treated glass/ITO substrates at 1000 rpm for 5 s and 5000 rpm for 30 s, and 200 µL CB was dropped on the spinning substrate 20 s before the end of the spin-coating process. The substrates were immediately transferred to the hotplate and annealed at 100 °C for 20 min. The surface passivation treatment procedure is consistent with the method mentioned above. The devices were finished by thermally evaporating C_{60} (25 nm), BCP (6 nm) and silver (100 nm) in sequential order.

0.9 M perovskite precursor solution $Cs_{0.05}(FA_{0.98}MA_{0.02})_{0.95}Pb(I_{0.98}Br_{0.02})_3$ was used for blade-coating of 1.55 eV cells. For the target device, Me-4PACz was added to the perovskite precursor. Then, the perovskite precursor solution is blade-coated on UV-ozone treated glass/ITO substrate

(the blading speed is 10 mm s^{-1} and the distance between the blade-coater and substrate is 100 μm) at room temperature in ambient air with a relative humidity of ~40%. Next, the as-prepared perovskite substrate was pretreated in a vacuum (<20 Pa) for 5 min, then transferred to the hotplate and annealed at 100 ℃ for 60 min. The surface passivation treatment procedure is consistent with the method mentioned above. The 1 cm^2 devices were finished by thermally evaporating C_{60} (25 nm), BCP (6 nm), and silver (100 nm) in sequential order.

For the devices fabricated by conventional "layer-by-layer" method using EADR03 or Br-2EPT molecule, the molecules were dissolved in IPA with a concentration of 0.25 mg/mL. EADR03 solution was heated to 60 ℃ to increase solubility. The as-prepared solution was spin-coated onto the UV-ozone treated ITO substrate at 4000 rpm for 30 s, then annealing at 100 °C for 10 min. The substrates were then washed with IPA through spin-coating at 4000 rpm for 30 s, followed by annealing at 100 °C for 5 min. 1.7 M $Cs_{0.05}(FA_{0.98}MA_{0.02})_{0.95}Pb(I_{0.98}Br_{0.02})_3$ perovskite precursor solution dissolved in mixed solvent (DMF/DMSO = 4:1 v/v) was spin-coated on the as-prepared substrates at 1000 rpm for 10 s, and 5000 rpm for 40 s, and 200 μL CB was dropped on the spinning substrate 10 s before the end of the spin-coating process. The substrates were immediately transferred to the hotplate and annealed at 100 °C for 30 min. For the devices with one-step coating process, EADR03 or Br-2EPT was added in perovskite precursor with a concentration of 0.25 mg/mL. In a typical procedure, the perovskite precursor containing EADR03 or Br-2EPT was spin-coated on UV-ozone treated glass/ITO substrates at 1000 rpm for 10 s and 5000 rpm for 40 s, and 200 μL CB was dropped on the spinning substrate 10 s before the end of the spin-coating process. The substrates were immediately transferred to the hotplate and annealed at 100 °C for

60 min. The devices were finished by thermally evaporating C_{60} (25 nm), BCP (6 nm) and silver (100 nm) in sequential order.

For the PSCs fabricated using EtOH-based solvent, 1.55 M $FA_{0.98}MA_{0.02}Pb(I_{0.98}Br_{0.02})_3$ perovskite precursor was prepared by mixing FAI, $PbBr_2$, PbI_2, and $PbBr_2$, with addition of 30 mol% MACl, 20 mol% PMACl, in a mixed solvent of EtOH and DMA (2:1 v/v). The perovskite precursor solution was heated to 60 ℃ for 1 h. Me-4PACz was added in perovskite precursor with a concentration of 0.25 mg/mL. The hole-selective contact and perovskite absorber were cast in a single coating step in a nitrogen glovebox. In a typical procedure, the perovskite precursor containing Me-4PACz was spin-coated on UV-ozone treated glass/ITO substrates at 5000 rpm for 30 s with gentle nitrogen air flow. The coated films were annealed at 100 °C for 20 min. The surface passivation treatment procedure is consistent with the method mentioned above. The devices were finished by thermally evaporating C_{60} (25 nm), BCP (6 nm) and silver (100 nm) in sequential order.

For the PSCs fabricated using ACN and 2-ME mixed solvent, 1 M $FA_{0.98}MA_{0.02}Pb(I_{0.98}Br_{0.02})_3$ perovskite precursor solution was prepared by mixing FAI, $PbBr_2$, PbI_2, $PbBr_2$ into a mixed solvent of ACN (60%, v/v)/2-ME (40%, v/v). The perovskite precursor solution needs to be heated to 60 ℃ for 1 h. Me-4PACz was added in perovskite precursor with a concentration of 0.25 mg/mL. Then, the perovskite precursor solution was blade-coated on the UV-ozone treated substrate (the blading speed is 10 mm s^{-1} and the distance between blade-coater and the substrate is 100 μm) at room temperature in ambient air with a relative humidity of ~40%. Next, the as-prepared perovskite substrate was pretreated in vacuum (<20 Pa) for 5 min, then transferred to the hotplate

at 100 ℃ for 20 min. The surface passivation treatment procedure is consistent with the method mentioned above. The devices were finished by thermally evaporating C_{60} (25 nm), BCP (6 nm) and silver (100 nm) in sequential order.

Material characterizations. The SEM images were taken using a Hitachi 4800 scanning electron microscope. The absorption spectra were obtained by a Shimadzu UV-3600 spectrophotometer. An ION-TOF TOF-SIMS V Time of Flight SIMS (TOF-SIMS) spectrometer was used for depth profiling of the perovskite films according to our previous report[51]. Depth Profiling was completed with a 30 KeV Bi_3^+ Bismuth primary ion beam (0.8 pA pulsed current rastered over a 50 × 50 μm area) and a 1 kV oxygen ion sputter beam (7 nA sputter current) rastered over a 150 × 150 μm area. Photoelectron spectroscopy measurements were conducted in a PHI 5600 UHV system. UPS and XPS measurements both employed an 11 in. diameter hemispherical electron energy analyzer and multichannel detector. The excitation source for UPS was an Excitech H Lyman-α lamp (E-LUXTM121) with excitation energy of 10.2 eV. All UPS measurements were recorded with -5 V sample bias and a pass energy of 5 eV. XPS measurements used an Al Kα x-ray excitation source (1486.6 eV) and a pass energy of 30 eV. TRPL measurements were made using an NKT supercontinuum laser (SuperK EXU-6-PP) used for excitation while a Hamamatsu C-10910-04 streak camera was used for detection (the fluence is 1.04 microwatts/square millimeter at 0.305 MHz and the wavelength is 532 nm).

Excitation at 632.8 nm (HeNe laser) was used to measure PL emission spectra. A Princeton Instruments HRS300 spectrograph with Si CCD (Pixis F100) and InGaAs (PyLoN IR) detectors was used. The spectral response of the detectors and spectrometer system was corrected using

calibration sources (IntelliCal for vis and IR ranges, Princeton Instruments) and placing calibration sources at the sample position. Excitation beam size was determined with a CCD camera. Data was measured in absolute photon numbers using Spectralon reflectance standards (LabSphere Inc.) and assuming that one-sun equivalent fluence for 1.68 eV bandgap is about 1.43×10^{17} photons/(cm^2s). The quasi-Fermi level splitting (QFLS) was determined from the spectral fit to the high energy side of the absolute PL emission spectrum[52].

The KPFM and c-AFM measurements were performed inside an Ar-filled glovebox. The devices were cleaved from the film side to expose the cross section for KPFM measurements, and the front side of the device was grounded, and bias voltage was applied from the back contact of the devices. KPFM measurements were performed with varying bias voltage from -1 V to +1 V on the same area. AFM images were taken on a Veeco Nanoscope IIIA instrument running in tapping mode.

Device characterizations. Simulated AM 1.5G irradiation (100 mW/cm^2) was produced by an Oriel Sol3A Class AAA Solar Simulator in a nitrogen glovebox for current density-voltage (*J-V*) measurements. The intensity of the solar simulator was calibrated with a KG5 filtered Si reference solar cell that was certified by NREL PV Performance Characterization Team, and the spectral mismatch factor was minimized to 0.9923. The device area was 0.122 cm^2 and was masked with a metal aperture to define an active area of 0.0585 cm^2. The scanning rate was 0.34 V s^{-1}. The stabilized power output (SPO) of the devices was measured by monitoring the photocurrent current density output with the biased voltage set near the maximum power point. External quantum efficiency (EQE) measurements were taken using a Newport Oriel IQE200. The devices made at City U. of Hong Kong were measured by an Enlitech SS-F5 solar simulator (calibrated to 100 mW

516 cm^{-2} by a silicon reference cell) for *J-V* measurements and an Enlitech QE-R system for EQE
517 measurements. The long-term operational stability was conducted by applying the PSCs under 1
518 sun equivalent LED lamp in a N_2-filled glovebox (with the contents of O_2 and H_2O <10 ppm). The
519 device operating temperature was measured to be ~40-45 ºC. The PSCs were biased at maximum-
520 power-point (MPP) voltage and the power output was tracked by using a multi-potentiostat
521 (CHI1040C, CH Instruments, Inc.). During the MPP test, the *J-V* curves of the devices were
522 obtained every 12 h to get the proper loads for the MPP.
523
524 **Computation.** DFT calculations were performed using the VASP code with projector augmented-
525 wave potentials[53-55]. A kinetic energy cutoff of 500 eV was used to expand the wave functions.
526 The Brillouin zone was sampled with Γ-centered 2×2×1 k-mesh. The atomic coordinates were
527 relaxed with PBE functional with a force tolerance of 0.01 eV $Å^{-1}$[56]. To model ITO, we used the
528 In_2O_3 crystal structure with 1/3 In atoms replaced by Sn. (222) surface was adopted with O
529 termination (passivated with H).
530
531 **Data availability**
532 The main data supporting the findings of this study are available within the article and its
533 Supplementary Information. Additional data are available from the corresponding authors on
534 reasonable request.
535
536 **References**

537 1. Jeon, N.J. et al. Compositional engineering of perovskite materials for high-performance
538 solar cells. *Nature* **517**, 476-480 (2015).
539 2. Jeon, N.J. et al. Solvent engineering for high-performance inorganic–organic hybrid
540 perovskite solar cells. *Nat. Mater.* **13**, 897-903 (2014).

3. Zhang, H. et al. A universal co-solvent dilution strategy enables facile and cost-effective fabrication of perovskite photovoltaics. *Nat. Commun.* **13**, 89 (2022).
4. Min, H. et al. Efficient, stable solar cells by using inherent bandgap of α-phase formamidinium lead iodide. *Science* **366**, 749-753 (2019).
5. Swarnkar, A. et al. Quantum dot–induced phase stabilization of α-$CsPbI_3$ perovskite for high-efficiency photovoltaics. *Science* **354**, 92-95 (2016).
6. Kim, M. et al. Conformal quantum dot–SnO_2 layers as electron transporters for efficient perovskite solar cells. *Science* **375**, 302-306 (2022).
7. Peng, J. et al. Centimetre-scale perovskite solar cells with fill factors of more than 86 per cent. *Nature* **601**, 573-578 (2022).
8. Chen, S. et al. Stabilizing perovskite-substrate interfaces for high-performance perovskite modules. *Science* **373**, 902-907 (2021).
9. Li, X. et al. Constructing heterojunctions by surface sulfidation for efficient inverted perovskite solar cells. *Science* **375**, 434-437 (2022).
10. Zhang, F. et al. Metastable Dion-Jacobson 2D structure enables efficient and stable perovskite solar cells. *Science* **375**, 71-76 (2022).
11. Luo, D. et al. Enhanced photovoltage for inverted planar heterojunction perovskite solar cells. *Science* **360**, 1442-1446 (2018).
12. Jiang, Q. et al. Surface passivation of perovskite film for efficient solar cells. *Nat. Photon.* **13**, 460-466 (2019).
13. Zheng, X. et al. Managing grains and interfaces via ligand anchoring enables 22.3%-efficiency inverted perovskite solar cells. *Nat. Energy* **5**, 131-140 (2020).
14. Jeong, J. et al. Pseudo-halide anion engineering for α-$FAPbI_3$ perovskite solar cells. *Nature* **592**, 381-385 (2021).
15. Wang, R. et al. Constructive molecular configurations for surface-defect passivation of perovskite photovoltaics. *Science* **366**, 1509-1513 (2019).
16. Wang, L. et al. A Eu^{3+}-Eu^{2+} ion redox shuttle imparts operational durability to Pb-I perovskite solar cells. *Science* **363**, 265-270 (2019).
17. Bai, S. et al. Planar perovskite solar cells with long-term stability using ionic liquid additives. *Nature* **571**, 245-250 (2019).
18. Wu, W.-Q. et al. Molecular doping enabled scalable blading of efficient hole-transport-layer-free perovskite solar cells. *Nat. Commun.* **9**, 1625 (2018).
19. Zhou, Z. et al. Organic/Inorganic Hybrid p-Type Semiconductor Doping Affords Hole Transporting Layer Free Thin-Film Perovskite Solar Cells with High Stability. *ACS Appl. Mater. Interfaces* **11**, 22603-22611 (2019).
20. Ye, S. et al. A Strategy to Simplify the Preparation Process of Perovskite Solar Cells by Co-deposition of a Hole-Conductor and a Perovskite Layer. *Adv. Mater.* **28**, 9648-9654 (2016).
21. Zhou, Z. & Pang, S. Highly efficient inverted hole-transport-layer-free perovskite solar cells. *J. Mater. Chem. A.* **8**, 503-512 (2020).
22. Al-Ashouri, A. et al. Conformal monolayer contacts with lossless interfaces for perovskite single junction and monolithic tandem solar cells. *Energy Environ. Sci.* **12**, 3356-3369 (2019).
23. Al-Ashouri, A. et al. Monolithic perovskite/silicon tandem solar cell with >29% efficiency by enhanced hole extraction. *Science* **370**, 1300-1309 (2020).

24. Levine, I. et al. Charge transfer rates and electron trapping at buried interfaces of perovskite solar cells. *Joule* **5**, 2915-2933 (2021).
25. Liu, J. et al. 28.2%-efficient, outdoor-stable perovskite/silicon tandem solar cell. *Joule* **5**, 3169-3186 (2021).
26. Jiang, Q. et al. Surface reaction for efficient and stable inverted perovskite solar cells. *Nature* **611**, 278-283 (2022).
27. Li, G. et al. Structure and Performance Evolution of Perovskite Solar Cells under Extreme Temperatures. *Adv. Energy Mater.* **12**, 2202887 (2022).
28. Cassella, E.J. et al. Gas-Assisted Spray Coating of Perovskite Solar Cells Incorporating Sprayed Self-Assembled Monolayers. *Adv. Sci.* **9**, e2104848 (2022).
29. Shi, W. & Ye, H. Efficient and Stable Perovskite Solar Cells with a Superhydrophobic Two-Dimensional Capping Layer. *J. Phys. Chem. Lett.* **12**, 4052-4058 (2021).
30. Chen, H. et al. Quantum-size-tuned heterostructures enable efficient and stable inverted perovskite solar cells. *Nat. Photon.* **16**, 352-358 (2022).
31. Chen, S. et al. Crystallization in one-step solution deposition of perovskite films: Upward or downward? *Sci. Adv.* **7**, eabb2412 (2021).
32. Hotchkiss, P.J. et al. The Modification of Indium Tin Oxide with Phosphonic Acids: Mechanism of Binding, Tuning of Surface Properties, and Potential for Use in Organic Electronic Applications. *Acc. Chem. Res.* **45**, 337-346 (2012).
33. Xiao, C. et al. Junction Quality of SnO_2-Based Perovskite Solar Cells Investigated by Nanometer-Scale Electrical Potential Profiling. *ACS Appl. Mater. Interfaces* **9**, 38373-38380 (2017).
34. Jiang, C.-S. et al. Carrier separation and transport in perovskite solar cells studied by nanometre-scale profiling of electrical potential. *Nat. Commun.* **6**, 8397 (2015).
35. Park, S.M., Abtahi, A., Boehm, A.M. & Graham, K.R. Surface Ligands for Methylammonium Lead Iodide Films: Surface Coverage, Energetics, and Photovoltaic Performance. *ACS Energy Lett.* **5**, 799-806 (2020).
36. Stolterfoht, M. et al. Visualization and suppression of interfacial recombination for high-efficiency large-area pin perovskite solar cells. *Nat. Energy* **3**, 847-854 (2018).
37. Li, L. et al. Flexible all-perovskite tandem solar cells approaching 25% efficiency with molecule-bridged hole-selective contact. *Nat. Energy* **7**, 708-717 (2022).
38. Zhao, Y. et al. Molecular Interaction Regulates the Performance and Longevity of Defect Passivation for Metal Halide Perovskite Solar Cells. *J. Am. Chem. Soc.* **142**, 20071-20079 (2020).
39. Zheng, X., Alsalloum, A.Y., Hou, Y., Sargent, E.H. & Bakr, O.M. All-Perovskite Tandem Solar Cells: A Roadmap to Uniting High Efficiency with High Stability. *Acc. Mater. Res.* **1**, 63-76 (2020).
40. Kim, M., Schmitt, S.K., Choi, J.W., Krutty, J.D. & Gopalan, P. From Self-Assembled Monolayers to Coatings: Advances in the Synthesis and Nanobio Applications of Polymer Brushes. *Polymers* **7**, 1346-1378 (2015).
41. Cheng, H. & Hu, Y. Influence of chain ordering on frictional properties of self-assembled monolayers (SAMs) in nano-lubrication. *Adv. Colloid Interface Sci.* **171-172**, 53-65 (2012).
42. Pathak, A. et al. Disorder-derived, strong tunneling attenuation in bis-phosphonate monolayers. *J. Phys.: Condens. Matter* **28**, 094008 (2016).

43. Aktas, E. et al. Understanding the perovskite/self-assembled selective contact interface for ultra-stable and highly efficient p–i–n perovskite solar cells. *Energy Environ. Sci.* **14**, 3976-3985 (2021).
44. Aktas, E. et al. Role of Terminal Group Position in Triphenylamine-Based Self-Assembled Hole-Selective Molecules in Perovskite Solar Cells. *ACS Appl. Mater. Interfaces* **14**, 17461-17469 (2022).
45. Aktas, E., Jiménez-López, J., Azizi, K., Torres, T. & Palomares, E. Self-assembled Zn phthalocyanine as a robust p-type selective contact in perovskite solar cells. *Nanoscale Horiz.* **5**, 1415-1419 (2020).
46. Ullah, A. et al. Novel Phenothiazine-Based Self-Assembled Monolayer as a Hole Selective Contact for Highly Efficient and Stable p-i-n Perovskite Solar Cells. *Adv. Energy Mater.* **12**, 2103175 (2022).
47. Deng, Y. et al. Defect compensation in formamidinium–caesium perovskites for highly efficient solar mini-modules with improved photostability. *Nat. Energy* **6**, 633-641 (2021).
48. Deng, Y. et al. Tailoring solvent coordination for high-speed, room-temperature blading of perovskite photovoltaic films. *Sci. Adv.* **5**, eaax7537.
49. Vidal, R. et al. Assessing health and environmental impacts of solvents for producing perovskite solar cells. *Nat. Sustain.* **4**, 277-285 (2021).
50. Yun, H.-S. et al. Ethanol-based green-solution processing of α-formamidinium lead triiodide perovskite layers. *Nat. Energy* **7**, 828-834 (2022).
51. Zhao, Q. et al. High efficiency perovskite quantum dot solar cells with charge separating heterostructure. *Nat. Commun.* **10**, 2842 (2019).
52. Unold, T. & Gütay, L. in Advanced Characterization Techniques for Thin Film Solar Cells 151-175 (2011).
53. Kresse, G. & Furthmüller, J. Efficient iterative schemes for ab initio total-energy calculations using a plane-wave basis set. *Phys. Rev. B.* **54**, 11169-11186 (1996).
54. Kresse, G. & Furthmüller, J. Efficiency of ab-initio total energy calculations for metals and semiconductors using a plane-wave basis set. *Comput. Mater. Sci.* **6**, 15-50 (1996).
55. Blöchl, P.E. Projector augmented-wave method. *Phys. Rev. B.* **50**, 17953-17979 (1994).
56. Perdew, J.P., Burke, K. & Ernzerhof, M. Generalized Gradient Approximation Made Simple. *Phys. Rev. Lett.* **77**, 3865-3868 (1996).

Acknowledgments

This work was authored in part by the National Renewable Energy Laboratory, operated by Alliance for Sustainable Energy, LLC, for the U.S. Department of Energy (DOE) under Contract No. DE-AC36-08GO28308. NREL acknowledges support from by the U.S. Department of Energy's Office of Energy Efficiency and Renewable Energy (EERE) under the Solar Energy Technologies Office (SETO) project "De-risking Halide Perovskite Solar Cells" program (DE-

FOA-0000990) for improved manufacturability aspects of perovskite solar cells and support from the Operational Energy Capability Improvement Fund (OECIF) of the Department of Defense for the initial concept. DFT calculations and TRPL acknowledge the support of the Center for Hybrid Organic Inorganic Semiconductors for Energy (CHOISE), an Energy Frontier Research Center funded by the Office of Basic Energy Sciences, Office of Science within the US Department of Energy. The work at City University of Hong Kong was supported by Innovation and Technology Fund (GHP/100/20SZ, GHP/102/20GD, MRP/040/21X) and Green Tech Fund (GTF202020164). This work was authored in part by the École Polytechnique Fédérale de Lausanne (EPFL), operated by NPRP grant No. NPRP11S-1231-170150 from the Qatar National Research Fund (a member of Qatar Foundation) and the VALAIS ENERGY DEMONSTRATORS FUND. T.L., H.P., and K.R.G. acknowledge funding from the National Science Foundation under awards OIA-1929131 (T.L. and K.R.G) and 2102257 (H.P. and K.R.G). The work at Brown University was supported by the Office of Naval Research (Grant No. N00014-20-1-2574), and by the U.S. DOE's Office of Energy Efficiency and Renewable Energy (EERE) under the Solar Energy Technology Office (SETO) Award No. DE-0009511. The views expressed in the article do not necessarily represent the views of the DOE or the U.S. Government.

Author contributions

J.M.L and X.Z. conceived the idea and designed the experiments. J.M.L. and Z.Z. supervised the project. X.Z. and Z.L. fabricated the devices and conducted the characterizations. Y.Z., D.G. and C.Z. participated in device fabrication. M.C., J.B.P., R.A.S, D.M., D.K., and B.M.W. performed optical spectroscopy and analysis. T.L. and H.P. carried out XPS and UPS measurements. C.X. conducted and analyzed the KPFM and C-AFM. S.P.H. performed TOF-SIMS. Z.L., Z.D. and N.P.P. contributed to the device MPP stability test. X.W. and Y.Y. performed and interpreted the

DFT calculation. A.M., A.R.K., N.P.P., Y.Y., K.R.G., M.K.N., M.C.B., and M.D.M. contributed to the analysis and provided advice. X.Z. and J.M.L. wrote the initial draft and all authors contributed to the final manuscript.

Competing interests

An application (No. 63/363,327) has been made for a provisional patent. M.D.M is an advisor to Swift Solar. The other authors declare no other competing interests.